AIAA JOURNAL
Vol. 30, No. 12, December 1992

Crossflow Aerodynamic Characteristics of a Noncircular Cylinder With and Without Strakes

Bandu N. Pamadi*
Vigyan Research Associates, Inc., Hampton, Virginia 23666
and
B. H. Laxmana Gowda†
Indian Institute of Technology, Madras 600036, India

The installation of a pair of thin strakes on the windward side of a flat-faced noncircular cylinder in axial flow at subcritical Reynolds numbers produced substantial changes in the flow pattern, vortex shedding, and drag coefficient. A particular strake configuration resulted in drag reduction of the order of 80%. In this paper, the effects of crossflow angle on drag and lift coefficients of this model are investigated with the help of pressure measurements in a low-speed wind tunnel and flow-visualization tests in a water tunnel. It is found that the drag and lift coefficients of the basic model (no strakes) vary significantly with the crossflow angle, assuming multiple maxima and minima. For a model with strakes, the influence of strakes on the flow pattern and the drag and lift coefficients becomes prominent as the crossflow angle increases.

Nomenclature

b_o = width of the model
C_D = drag coefficient, $\dfrac{\text{drag force per unit length}}{\frac{1}{2}\rho V_\infty^2 b_o}$
C_{Do} = drag coefficient of the basic shape, $C_{xo}\cos\phi - C_{yo}\sin\phi$
C_{Dt} = total drag coefficient, $C_{Do} + \Delta C_{DS}$
C_L = lift coefficient, $\dfrac{\text{lift force per unit length}}{\frac{1}{2}\rho V_\infty^2 b_o}$
C_{Lo} = lift coefficient of the basic shape, $C_{xo}\sin\phi + C_{yo}\cos\phi$
C_{Lt} = total lift coefficient, $C_{Lo} + \Delta C_{LS}$
C_p = pressure coefficient, $\dfrac{p - p_\infty}{\frac{1}{2}\rho V_\infty^2}$
C_{pb} = base pressure coefficient
C_x = axial force coefficient, $\dfrac{\text{axial force per unit length}}{\frac{1}{2}\rho V_\infty^2 b_o}$
C_{xo} = axial force coefficient of basic shape
C_y = cross force coefficient = $\dfrac{\text{cross force per unit length}}{\frac{1}{2}\rho V_\infty^2 b_o}$
C_{yo} = cross force coefficient of the basic shape
h = strake height
p = pressure
s = distance measured along the strake
V_∞ = freestream velocity
ΔC_{DS} = drag coefficient of strakes, $-(\Delta C_{y1} + \Delta C_{y2})\sin\phi$
ΔC_{LS} = lift coefficient of strakes, $(\Delta C_{y1} + \Delta C_{y2})\cos\phi$
ΔC_{yS} = total cross force coefficient of the strakes, $\Delta C_{y1} + \Delta C_{y2}$
ΔC_{y1} = cross force coefficient of strake S_1
ΔC_{y2} = cross force coefficient of strake S_2
η = nondimensional strake location, r/b_o
θ = angle measured to a given point on the model surface from the centerline, deg
ξ = nondimensional stake height, h/b_o
ϕ = crossflow angle, deg

Presented as Paper 88-2599 at the AIAA 6th Applied Aerodynamics Conference, Williamsburg, VA, June 6-8, 1988; received May 7, 1990; revision received March 23, 1992; accepted for publication March 23, 1992.

*Senior Scientist, 30 Research Drive. Senior Member AIAA.
†Professor, Department of Applied Mechanics.

Introduction

THE flow around two-dimensional bluff, noncircular cylinders in crossflow has always attracted the attention of aerodynamicists. At subcritical Reynolds numbers, the flow over such bodies is characterized by a large wake, strong periodic (Karman-type) vortex shedding, and a high value of drag coefficient. A popular method of reducing the drag of such bodies is to round off the sharp corners.[1,2] However, the maximum drag reduction achievable by this technique appears to be limited to 50%.[2] Recently, authors have proposed a new method that is capable of achieving higher drag reduction.[3] This method consists of installing a pair of thin strakes on the windward face of the noncircular cylinder. With this approach, drag reduction of 81.5% was obtained for a certain strake configuration (called optimum configuration) in axial flow. An application of this technique to road transport vehicles is discussed in Ref. 4.

The fluid flow mechanism that produced such large drag reduction was identified as the one in which the flow separates at the strakes, undergoes transition to turbulence, and then smoothly reattaches back to the body at or very close to the corners (Fig. 1a). A separation bubble is formed between the strakes and the reattachment point, and this bubble generates suction on the forward face. The vortex shedding was greatly suppressed, and drag reduction of about 81.5% occurred.[3] Koenig and Roshko[5] found that a disk mounted in front of a flat-faced axisymmetric cylinder produced significant drag reductions for some combinations of disk diameter (d_1/d_2) and gap (g/d_2) ratios (Fig. 1b). The flow mechanism associated with drag reduction was the smooth reattachment of the separated shear layers originating at the edges of the disk back to the cylinder at or very close to the shoulder (Fig. 1b). Thus, the primary flow mechanisms leading to optimum drag reductions appear to be of the same nature in two-dimensional and axisymmetric flows.

The purpose of this paper is to investigate the effects of crossflow angle on the flow pattern and the drag and lift coefficients of the noncircular cylinder of Ref. 3 with and without strakes. Extensive pressure measurements in a low-speed, low-Reynolds-number wind tunnel have been performed for crossflow angles from 0 to 90 deg. Some flow-visualization tests in a water tunnel were conducted to help the interpretation of the wind-tunnel pressure test data. The variation of crossflow angle produced interesting results. A small change in the crossflow angle (7 deg) did not alter the flow

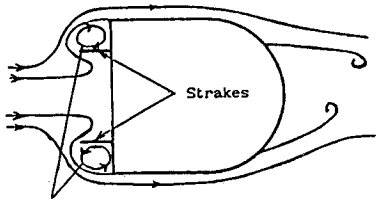

a) Two-dimensional flow over noncircular cylinder with strakes[3]

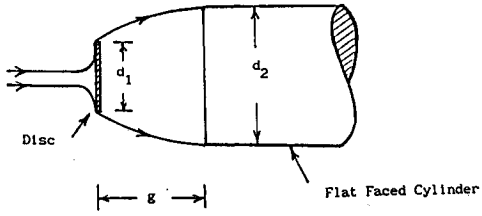

b) Axisymmetrical flow over flat-faced cylinder with disk[4]

Fig. 1 Flow patterns for optimum drag reductions.

pattern and drag coefficient of the optimum strake configuration. With further increase in crossflow angle, the drag coefficient increased rapidly. For basic model (no strakes) and other strake configurations, the drag coefficient dropped significantly for a small value of crossflow angle. The drag and lift coefficients assume multiple minima and maxima at various crossflow angles.

Experimental Work

Pressure Distribution Tests

These tests were carried out in a 2- × 2-ft (61- × 61-cm) low-speed, closed-jet, open-circuit wind tunnel having a maximum velocity of 115 ft/s (35 m/s). The test model is the same as that employed in Ref. 3. The cross section of the model consists of three flat sides and a semicircular top, as shown in Fig. 2. The model is so held that in axial flow ($\phi = 0$) the flat side with sharp corners faces the airstream and the rounded top is on the lee side. The test cylinder spanned the horizontal dimension of the wind-tunnel test section. In this way, the effective aspect ratio of the model is theoretically equal to infinity. The orifices that were used to measure the pressure distribution over the model were located at the midplane. Two additional sets of pressure orifices were also installed half the way between the tunnel walls and the midplane to continuously monitor the existence of a true, two-dimensional flow over the model. At test conditions, the side wall boundary layer had a displacement thickness of about 0.25 in., which is quite small and negligible compared to the horizontal dimension of the test section (2 ft). More details of the test model are available in Ref. 3.

Pressure distribution was measured for a basic model (no strakes) and a model with strakes. The strake geometry is characterized by two parameters: the nondimensional strake height $\xi = h/b_o$, and the nondimensional distance $\eta = r/b_o$. Here r is the distance from the model corner to the strake location (Fig. 2). Tests were carried out for $\xi = 0.1$, 0.2, and 0.3 with η varying from 0 to 0.5 in steps of 0.1. Note that for $\eta = 0.5$ only one strake was installed. In this paper, typical results for the basic model and the model with strakes of height $\xi = 0.3$ are presented. Additional results are available in Ref. 6. To measure the pressure distribution over the strakes ($\xi = 0.3$), three pressure taps were installed on either side of the strakes, as shown schematically in Fig. 2. The crossflow angle ϕ generally varied in steps of 5 deg from 0 to 90 deg for the basic model and 0–70 deg for the model with strakes. For the optimum strake configuration ($\xi = 0.3$ and $\eta = 0.2$), ϕ was varied in steps of 1 deg from 0 to 10 deg. The Reynolds number based on the model width b_o was close to 10^5, which falls in the subcritical range for the subject cross section.[7] The test results are corrected for wind-tunnel blockage effects.

Errors and Uncertainties

The crossflow angle was measured within ± 0.25 deg. The pressures were read on a manometer with an accuracy of ± 0.25 mm of alcohol. For these values of measurement uncertainties, a detailed analysis using the method of Ref. 8 was performed to determine the uncertainties in pressure and force coefficients. The uncertainty in C_p was found to be less than ± 3%. The mean and standard error of the mean of uncertainties in various other coefficients are as follows:

$WC_{Dt} = 0.0173 \pm 0.0006$, $WC_{Lt} = 0.0221 \pm 0.0004$,
$WC_{xo} = 0.0133 \pm 0.0003$, $WC_{yo} = 0.0157 \pm 0.0003$,
$W\Delta C_{y1} = 0.0122 \pm 0.0006$, $W\Delta C_{y2} = 0.0109 \pm 0.0006$,
$W\Delta C_{ys} = 0.0168 \pm 0.0007$, $W\Delta C_{Ds} = 0.0092 \pm 0.0008$,
$W\Delta C_{Ls} = 0.0127 \pm 0.0006$.

Here, WC_{Dt}, WC_{Lt}, etc., are the estimated uncertainty coefficients in C_{Dt}, C_{Lt} etc.

Flow Visualization Tests

These tests were carried out in a small water tank (2.5 × 1.5 × 0.15 m). The water flow in the tank is generated by two counter-rotating paddles installed at one end of the tank. The water flow is smoothly guided all along the two sides of the tank and then into the test section located in the center of the tank. The width of the test section was 0.35 m, and the depth of the water in the test section was 0.12 m. The test model had a width of 0.04 m. The velocity of the water stream in the test section was 0.15 m/s, giving a test Reynolds number of 6×10^3 based on model width. The flow visualization was performed at the free water surface using aluminum powder as the tracer medium. Because of this constraint of the free surface, there is a discontinuity in the fluid medium at the free surface where the flow visualization is performed. A possible source of error is due to the shear effect, which is proportional to the density ratio of air and water. Since this density ratio is small (0.001), the shear effects are ignored. Another possible source of error in free surface flow visualization is due to the finite depth of water flow, which in the present case is equal to 0.12 m. The local pressure distribution around the model causes this depth to vary and affect the two-dimensional nature of the flow. The maximum possible rise in water level occurs at the stagnation point and is equal to $V_\infty^2/2g$. With $V_\infty = 0.15$ m/s, $V_\infty^2/2g = 0.001$ m, which is about 0.83% of the water depth. Hence, the errors due to finite water depth are ignored. Another possible source of error arises due to the finite aspect ratio of the flow-visualization model. With model width of 0.04 m and test section width of 0.35 m, the aspect ratio equals 8.75. This value, however, is slightly below the usually accepted value of 10. Any errors due to this difference in aspect ratios are ignored.

Photographs were taken at $\phi = 0$, 30, and 60 deg by a 35-mm camera held above the free water surface. The flow-visualization Reynolds number of 6×10^3 is one order of magnitude smaller than that in the wind-tunnel tests (10^5). Therefore, it is possible that the flow over the wind-tunnel model differs from that observed in the flow-visualization tests. The flow-visualization data are used only for qualitative interpretations of the flow around the model frontal face and strakes

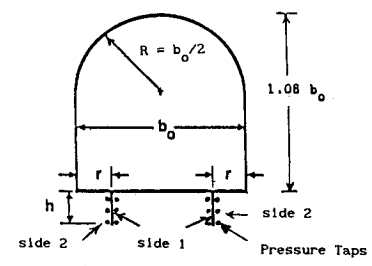

Fig. 2 Test model.

where the model sharp corners and sharp edges of the strakes have a greater influence and the difference in Reynolds numbers is a less significant factor.

Results

For the basic model and the model with strakes ($\xi = 0.3$), C_p plots are presented for $\phi = 0$, 15, 30, and 60 deg. Each of the

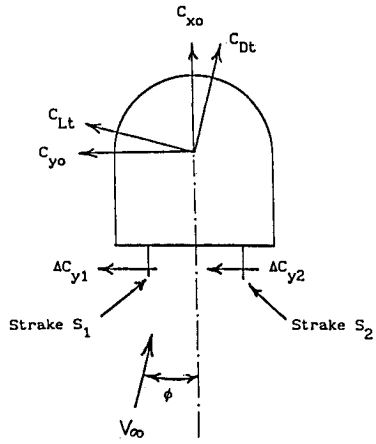

Fig. 3 Sectional aerodynamic forces on the model.

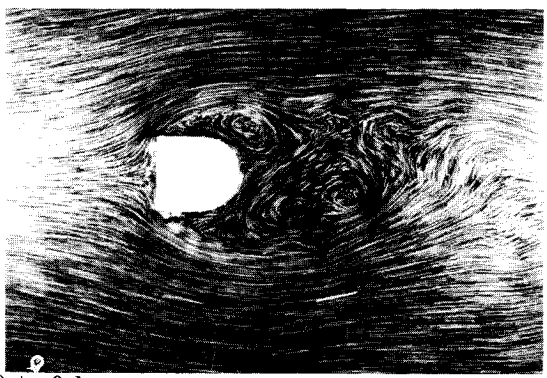

a) $\phi = 0$ deg

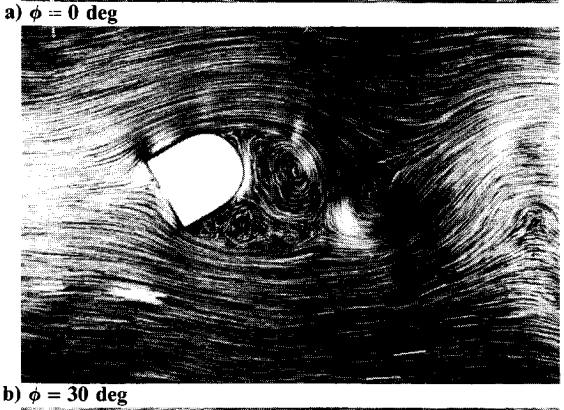

b) $\phi = 30$ deg

c) $\phi = 60$ deg

Fig. 4 Flow-visualization photographs of basic model.

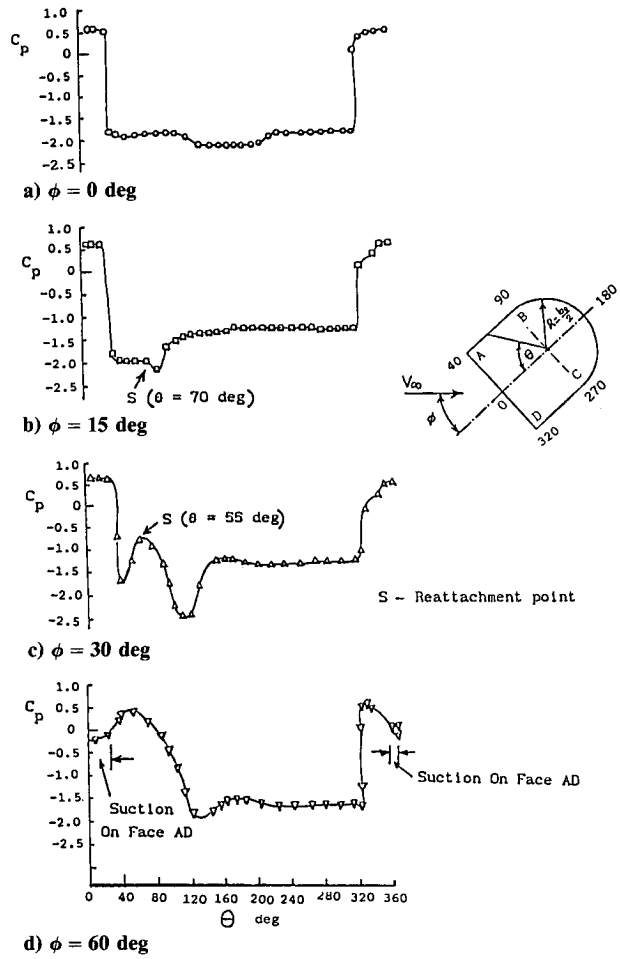

a) $\phi = 0$ deg

b) $\phi = 15$ deg

c) $\phi = 30$ deg

d) $\phi = 60$ deg

Fig. 5 Pressure distribution over basic model.

C_p plot is in two parts, part A gives the pressure distribution over the basic shape (model surface less strakes) and part B gives the pressure distribution on either side of the two strakes. The two sides of the strakes are labeled as side 1 and side 2, as shown in Fig. 2.

The aerodynamic force acting on the model cross section in two-dimensional axial flow can be resolved into various components, as shown in Fig. 3. The drag and lift coefficients can then be obtained as follows:

$$C_{Dt} = C_{xo} \cos \phi - (C_{yo} + \Delta C_{y1} + \Delta C_{y2}) \sin \phi \quad (1)$$

$$C_{Lt} = C_{xo} \sin \phi + (C_{yo} + \Delta C_{y1} + \Delta C_{y2}) \cos \phi \quad (2)$$

All of the force coefficients on the right-hand side of these equations were obtained by integrating the measured pressures over the corresponding surfaces. The axial force coefficient of strakes is ignored.

Discussion

Basic Model

The flow around the basic model at $\phi = 0$ is characterized by extensive wake. The wake flow is oscillatory because of strong, alternate, and periodic (Karman-type) vortex shedding (Fig. 4a). The separated shear layers feed large amounts of vorticity to the vortices that are continuously shed downstream. This process gives rise to a large wake, a high base suction with $C_{pb} = -2.2$ (Fig. 5a), and a high drag coefficient $C_d = 2.20$ (Fig. 6c). This value of drag coefficient is in good agreement with Obasaju,[9] who gives $C_D = 2.18$ for a square cylinder in subcritical axial flow. In the Reynold's number range of 10^4–10^5, such bluff bodies are known to exhibit strong vortex shedding[9] with the Strouhal number (fb_o/V_∞, f is the frequency of vortex shedding) varying from 0.12 to 0.14.

A direct study of the vortex shedding phenomenon was not attempted in this work.

With a small increase in ϕ, the shear layer separating at the windward corner (A) reattaches back to the body on the top side AB. (For convenience, the model's corners and surfaces have been labeled as shown in the insert to Fig. 5.) On the bottom side, flow remains separated. The reattaching streamline is incident on the top side AB (Fig. 4b). The flow reattachment is accompanied by a pressure rise, which can be identified in C_p plots (Figs. 5b and 5c). Initially, when ϕ is small, the reattachment point is located aft on the side AB but gradually moves toward the corner A as ϕ increases. For example, at $\phi = 15$ deg, the reattachment point is located at $\theta = 70$ deg and moves to $\theta = 55$ deg for $\phi = 30$ deg. Here, θ is the angle measured clockwise from the model centerline to a point on the body surface, as shown in the insert to Fig. 5.

With reattachment of the flow, suction on the upper side (AB plus one half of rounded side BC) increases compared to that on the lower side (CD plus the other half of rounded side BC). This leads to the development of the cross force, an increase in the base pressure, and a fall in the axial force coefficient. The axial and cross force coefficients C_{xo} and C_{yo} assume, respectively, minimum and maximum values at $\phi = 20$ deg leading to a minimum in the drag coefficient (Fig. 6). As ϕ increases further, the suction on the lower side increases due to the sharp turning of the flow at the corner (D). As a result, C_{yo} starts falling and C_{xo} shows a small rise. Hence, the lift coefficient C_{Lo} starts dropping and the drag coefficient C_{Do} registers a modest increase.

When ϕ is approximately equal to 45 deg, the adverse effect of the corner A, which caused flow separation at the lower values of ϕ, vanishes. The flow over the model is considerably smooth and streamlined. The drag coefficient drops to its second minimum at $\phi = 45$ deg. As ϕ increases above 45 deg, C_{yo} changes sign because positive pressures are formed on the side AB. The adverse effect of the corner A comes back at higher values of ϕ causing flow separation at corner A (Fig. 4c) and generation of suction on face AD (Fig. 5d). Because of the suction on the face AD, C_{xo} starts falling and even becomes negative for $\phi > 75$ deg. The decreases in C_{xo} and C_{yo} together contribute to the fall in C_{Do} and C_{Lo}. C_{Do} assumes its third minimum at $\phi = 85$ deg and C_{Lo} its second minimum at $\phi = 80$ deg. However, C_{Do} and C_{Lo} rise again as ϕ approaches 90 deg due to the increase in C_{xo} beyond ϕ values of 80 deg.

Strake Configurations

In Ref. 3, the flow patterns over the model with strakes at $\phi = 0$ where classified into three types called A, B, and C. The type A pattern occurred when the strakes were located at or close to the corners ($\eta = 0$, 0.1). The type B pattern occurred for only one strake configuration (optimum) with $\xi = 0.3$ and $\eta = 0.2$. The type C pattern occurred when the strakes were located closer to the center ($\eta = 0.3$–0.5). In this paper, the strake configurations with $\eta = 0$ and 0.4 are chosen as representatives of types A and C, respectively. The effect of cross-flow angle on these three types of flow patterns is discussed in the following.

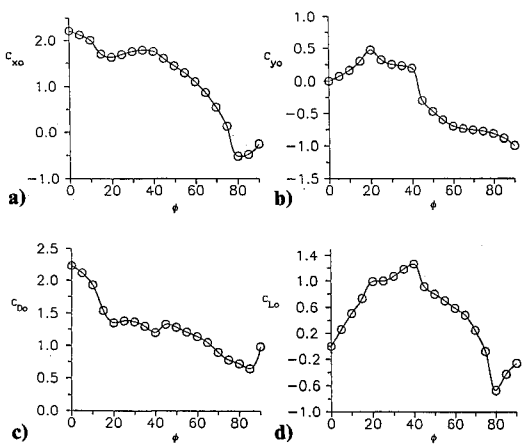

Fig. 6 Sectional aerodynamic coefficients of basic model.

Type A

In axial flow, the separated shear layers originating at the edges of the strakes open out forming a large wake with no subsequent reattachment to the model surface (Fig. 7a). The pressure in the region between the two strakes S_1 and S_2 is nearly constant. C_p varies smoothly across side 1 of each of the strakes. On side 2 of both of the strakes, C_p is nearly constant due to flow separation at the sharp edges of S_1 and S_2. Because of this flow separation, a strong, alternate, and periodic (Karman-type) vortex shedding occurs accompanied by high values of base suction (Fig. 8a for $\phi = 0$), axial force, and drag coefficients (Figs. 9a and 9c). For a small increase in ϕ above zero, the flow reattaches on side AB in a similar fashion to that observed for the basic model. This reattachment can be observed in the flow-visualization photograph of Fig. 7b and identified in C_p plots of Fig. 8a for $\phi = 15$ and 30 deg. As noted for the basic model, the reattachment of the flow leads to an increase in C_{pb}, a decrease in C_{xo}, and a build up of C_{yo}. At low values of ϕ, the cross force coefficients (ΔC_{y1} and ΔC_{y2}) on strakes S_1 and S_2 act in opposite directions

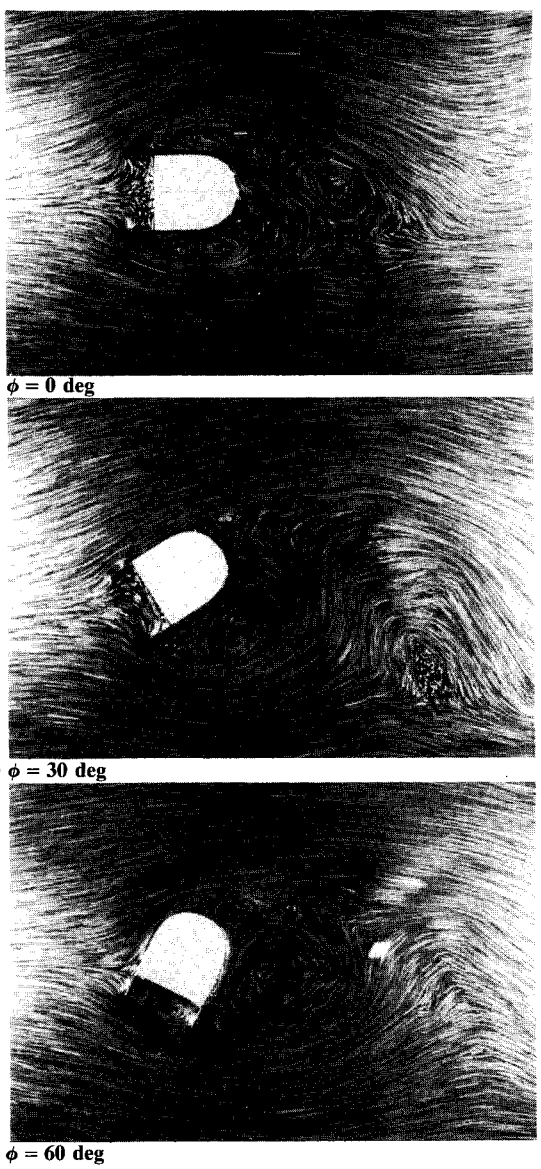

Fig. 7 Flow visualization photographs of type A pattern.

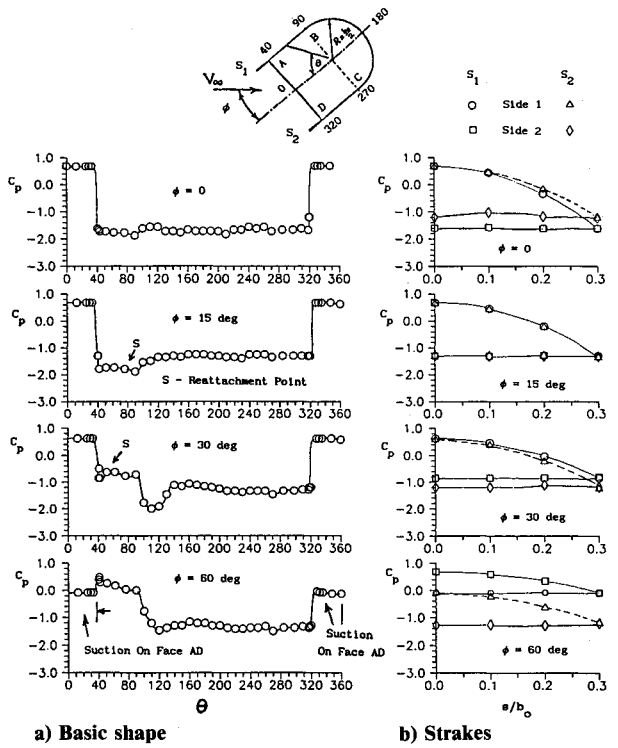

a) Basic shape b) Strakes

Fig. 8 Pressure distribution plots for the type A pattern.

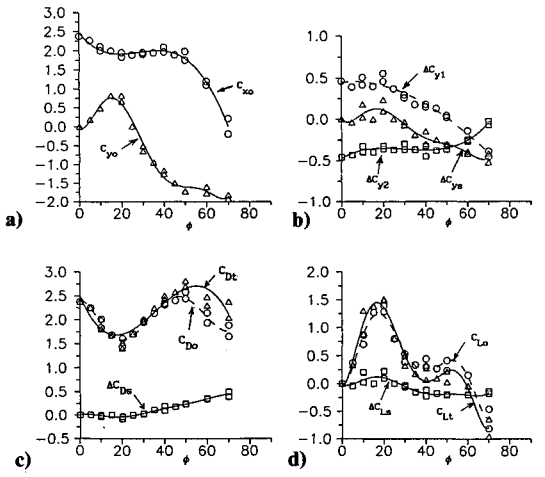

Fig. 9 Sectional aerodynamic coefficients of type A pattern.

(Fig. 9b) and, hence, the strakes contribution to total drag and lift coefficients (C_{Dt} and C_{Lt}) is small (Figs. 9c and 9d).

As ϕ increases, the reattachment point S was found to move toward the corner A in a similar fashion to that noted for the basic model. The sharp turning of the flow at S_2 generates considerable suction on side CD. As a result, C_{yo} starts falling. C_{xo} is not affected by the suction on side CD and therefore remains approximately constant in this process. Across the windward strake S_1, the pressure differential gradually reduces, resulting in a fall in ΔC_{y1}. ΔC_{y2} is almost constant for $20 < \phi < 40$ deg because of steady values of pressure differential across it. As a result, the total cross force coefficient of strakes (ΔC_{ys}) starts falling (Fig. 9b).

For $\phi > 45$ deg, positive pressures are formed on side AB and on the side 2 of the strake S_1 (Fig. 8b for $\phi = 60$ deg). A suction bubble is formed between strakes S_1 and S_2, as seen in the flow-visualization photograph of Fig. 7c and noted in the C_p plot of Fig. 8a for $\phi = 60$ deg. Because of this suction effect, C_{xo} and ΔC_{y1} fall steeply and ΔC_{y2} rises (Fig 9b). The sharp fall in C_{xo} contributes to a decrease in C_{Dt} even though ΔC_{Ds} is increasing (Fig. 9c). The falling of C_{xo}, C_{yo}, and ΔC_{yS} together cause C_{Lt} to decrease at high values of ϕ, as seen in Fig. 9d.

Type B

This flow pattern is characterized by a smooth, tangential flow reattachment at or very close to the windward corners, as observed in the flow-visualization photograph of Fig. 10a. (See Ref. 3 for more details.) After reattachment, the flow follows the model surface to a considerable extent and produces a substantial pressure recovery before finally separating from the body surface. The steep pressure recovery (Fig. 11a for $\phi = 0$) prior to the flow separation is typical of turbulent boundary-layer separation.[10] Based on this observation, it was speculated in Ref. 3 that the flow transition must have occurred prior to the flow reattachment. Another factor that contributes to the large drag reduction is the suction generated on the forward face due to the formation of bubbles between the strakes and corners. With the establishment of this flow pattern, the vortex shedding is considerably suppressed, as observed in Fig. 10a, and C_{Dt} assumes a value of 0.42 (Fig. 12c), which is the minimum for the subject model.[3] For an increase in ϕ up to 7 deg (in steps of 1 deg), C_{Dt} remains close to the minimum value of 0.42. The pressure distribution plots (not shown) for ϕ varying from 0 to 7 deg were identical to the one obtained at $\phi = 0$. This result is of considerable practical

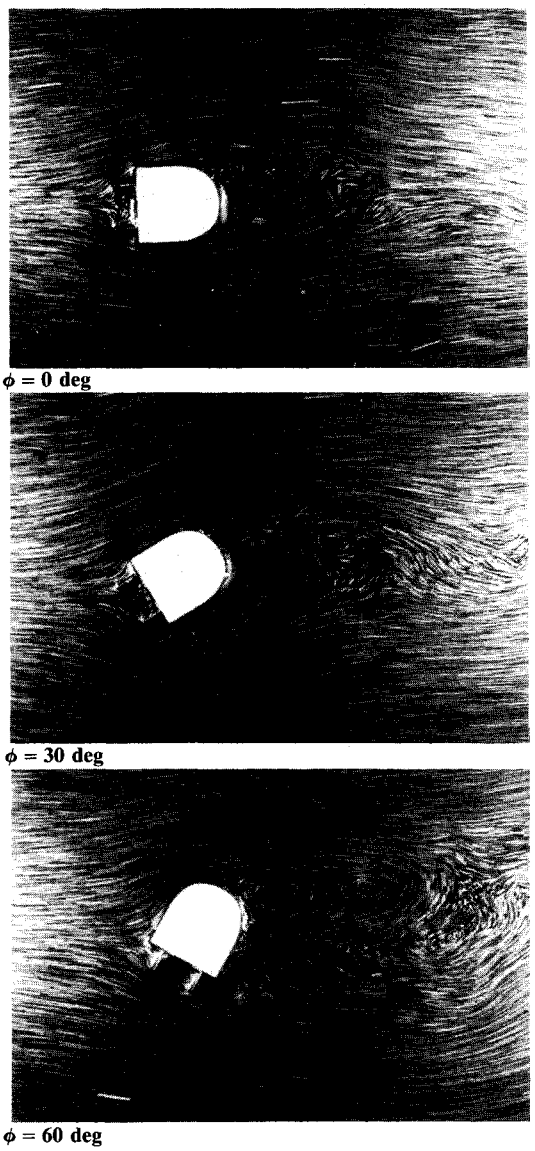

a) $\phi = 0$ deg

b) $\phi = 30$ deg

c) $\phi = 60$ deg

Fig. 10 Flow-visualization photographs of type B pattern.

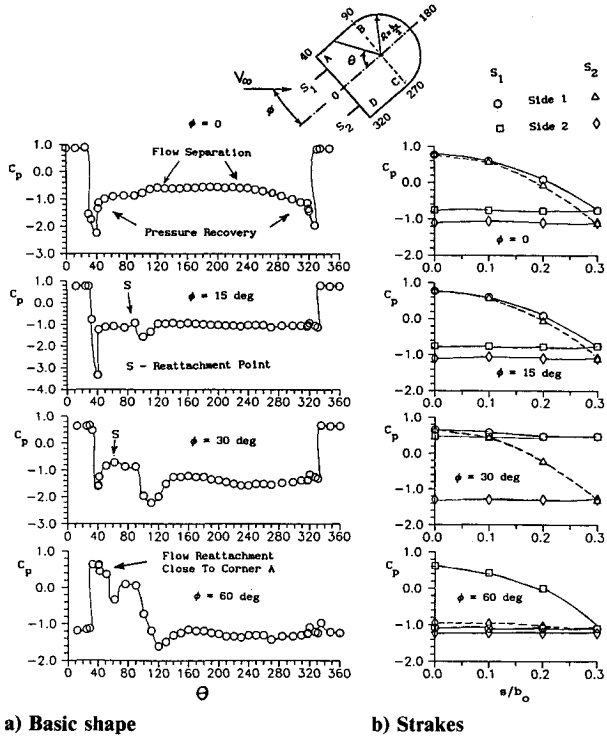

a) Basic shape b) Strakes

Fig. 11 Pressure distribution plots for type B pattern

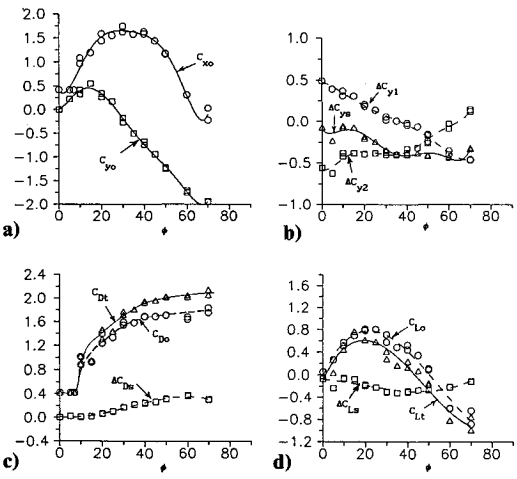

Fig. 12 Sectional aerodynamic coefficients of type B pattern.

significance. The bodies[4] employing this technique can have the benefit of drag reduction without requiring precision alignment with the flow direction.

For $\phi > 7$ deg, the smooth tangential reattachment of the flow is apparently lost. The reattaching free streamline is incident on the model top surface. The flow reattachment can be observed in Fig. 10b and identified by the pressure rise on the side AB in C_p plots of Fig. 11a for $\phi = 15$ and 30 deg. Such a flow reattachment where the free streamline is incident on the model surface leads to less base pressure recovery compared to the smooth tangential reattachment. (Compare $C_{pb} = -1.3$ at $\phi = 15$ deg with $C_{pb} = -0.6$ at $\phi = 0$.) As a result, C_{xo}, C_{Do}, and C_{Dt} start rising sharply. C_{yo} builds up initially and then falls off subsequently in a similar fashion to that observed for the basic model and type A pattern.

At low/moderate values of ϕ, ΔC_{ys} is negative because the flow turning at the lee side strake S_2 is sharper compared to that at the windward strake S_1 (Fig. 10b). A sharper flow turn generates a higher pressure differential and, hence, a larger cross force. As ϕ increases further, say $\phi > 40$ deg, the flow direction around the strake S_1 changes and positive pressures are formed on side 2 of S_1 (Fig. 11b for $\phi = 60$ deg). A suction bubble is formed between the strakes and, hence, ΔC_{y1} and C_{xo} fall and ΔC_{y2} rises. The fall in C_{xo} reduces C_{Do}, whereas the decrease in C_{yo} causes C_{Do} to rise. As a result, C_{Do} tends to level off at higher values of ϕ (Fig. 12c). ΔC_{Ds} is small at low values of ϕ but assumes significance at higher values of ϕ. C_{Lt} falls off at higher values of ϕ because C_{Lo} falls off rapidly (Fig. 12d).

Type C

At $\phi = 0$, the separated shear layers originating at the tip of the strakes reattach to the flat face of the model, as observed in the flow-visualization photograph of Fig. 13a and identified by the pressure rise in the C_p plot of Fig. 14a. But the flow cannot negotiate the sharp corners A and D and, hence, separates once again, forming a large wake with strong, alternate, and periodic (Karman-type) vortex shedding. The drag coefficient is high and close to the value of the basic model (Fig. 15c).

For a small increase in ϕ above zero, the flow that separated at corner A reattaches back to the surface AB, leading to a fall in C_{xo} and a development of C_{yo}, as observed for the basic model and the type A pattern. At low values of ϕ, the flow slides smoothly over the strake S_1 because the magnitude of the pressure differentials (Fig. 14b) for $\phi = 15$ deg and ΔC_{y1} are small (Fig. 15b). However, the flow turns sharply at strake S_2, producing substantial suction in the region between the

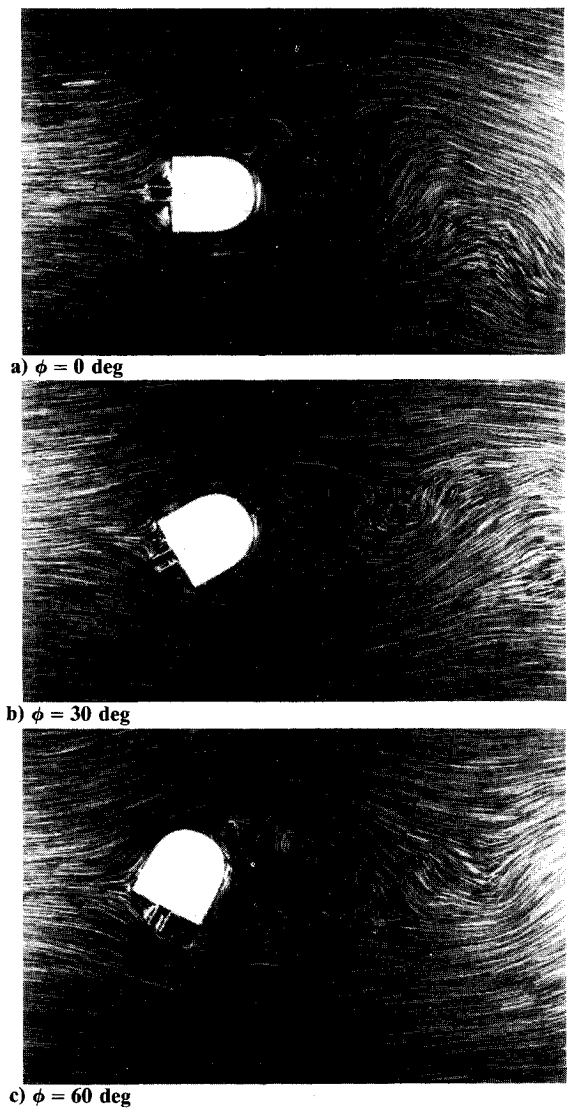

a) $\phi = 0$ deg

b) $\phi = 30$ deg

c) $\phi = 60$ deg

Fig. 13 Flow-visualization photographs of type C pattern.

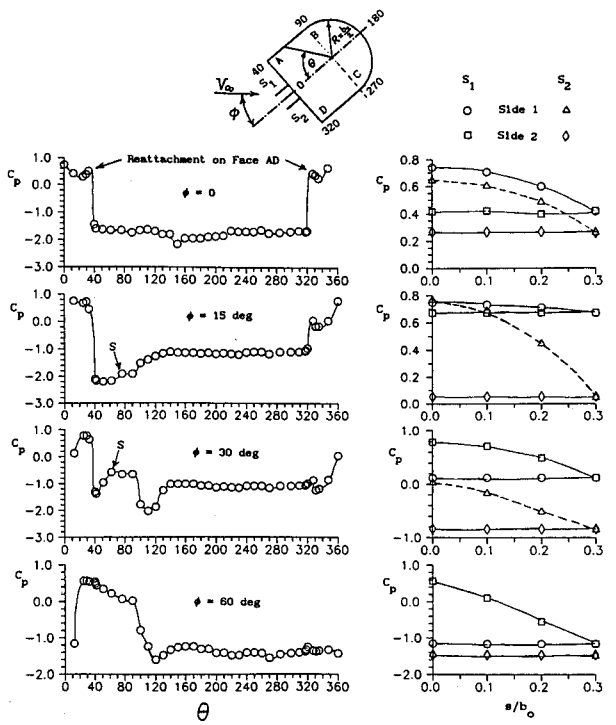

a) Basic shape b) Strakes

Fig. 14 Pressure distribution plots for type C pattern.

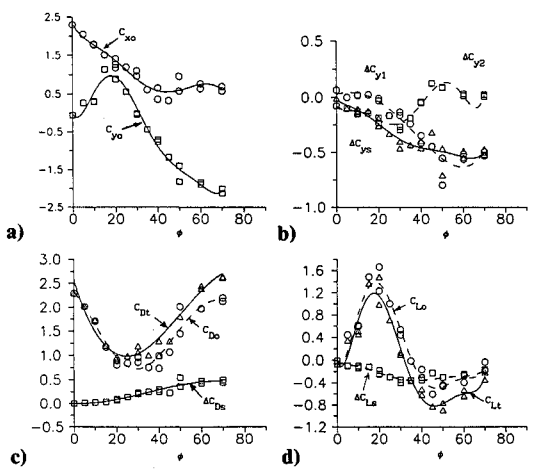

Fig. 15 Sectional aerodynamic coefficients of type C pattern.

strake S_2 and the corner D. This leads to a considerable negative value of ΔC_{y2} and a steep fall in C_{xo}. For $\phi > 20$ deg, flow direction around S_1 changes and positive pressures are formed on its side 2. As a result, ΔC_{y1} steadily falls and becomes negative.

For $\phi > 40$ deg, a separation bubble is formed and trapped between the strakes S_1 and S_2, as observed for type A and B patterns. Because of the suction created by this bubble, ΔC_{y1} falls and ΔC_{y2} rises. However, the bubble's influence on C_{xo} is less prominent compared to type A and B patterns because the space on which it acts is much smaller. Therefore, the steep fall in C_{xo} at high values of ϕ observed for type A and type B patterns is not observed here. Instead C_{xo} shows a modest rise, which together with the negative values of C_{yo} and ΔC_{ys} causes C_{Dt} to rise. C_{Lt}, which peaked around $\phi = 20$ deg and dropped subsequently, starts rising again for $\phi > 40$ deg due to the increasing contribution of strakes (Fig. 15d).

Concluding Remarks

The results of this study have brought out some interesting features of bluff body flows at subcritical Reynolds numbers. Simple geometrical modifications, such as the installation of a pair of strakes facing the airstream, can significantly change the flow pattern, vortex shedding, and drag and lift coefficients of flat-faced noncircular cylinders.

In the axial flow, three types of flow patterns, called A, B, and C, were identified for a certain flat-faced noncircular cylindrical model. The type B pattern produced a drag coefficient of 0.42, giving an optimum drag reduction of about 81.5%.

The variation of crossflow angle produced interesting results. For the basic model, a small value of crossflow angle leads to the reattachment of the flow on the top surface, an increase in base pressure, a sharp fall in the drag coefficient, and a quick buildup of lift coefficient. The drag and lift coefficients assume, respectively, their first minimum and maximum values at $\phi = 20$ deg. A second minimum in drag coefficient occured around $\phi = 45$ deg when the adverse effect of the windward corner vanishes to make the flow considerably smooth and streamlined. At higher crossflow angles, the drag coefficient drops again, assuming a third minimum at $\phi = 80$ deg due to the suction formed on the bottom surface.

For the type A and C patterns, a small value of crossflow angle produced flow reattachment followed by a sharp decrease in drag coefficient and a quick buildup of lift coefficient similar to those observed for the basic model. However, for the type B pattern, the smooth tangential reattachment of the flow found in axial flow and which produced an optimum drag reduction was lost for an increase in the crossflow angle beyond 7 deg leading to a sharp rise in the drag coefficient. The flow direction, pressure distribution, and cross forces over the strakes vary significantly with crossflow angle. At extreme crossflow angles, a suction bubble is formed and trapped between the strakes and influences the drag and lift coefficients of the model.

References

[1]Hoerner, S. F., *Fluid Dynamic Drag,* Hoerner, S. F., Bricktown, NJ, 1965, pp. 312, 313.

[2]Jorgensen, L. H., and Brownson, J. J., "Effect of Reynolds Number and Body Corner Radius on Aerodynamic Characteristics of a Space Shuttle Type Vehicle at Subsonic Mach Numbers," NASA TN D-6615, Jan. 1972.

[3]Pamadi, B. N., Pereira, C., and Laxmana Gowda, B. H., "Drag Reduction of Non Circular Cylinders by Strakes," *AIAA Journal*, Vol. 26, No. 3, 1988, pp. 292–299.

[4]Pamadi, B. N., Taylor, L. W., Jr., and Leary, T. O., "A Method for the Reduction of Aerodynamic Drag of Road Vehicles," NASA TM 102589, Jan. 1990.

[5]Koenig, K., and Roshko, A., "An Experimental Study of Geometrical Effects on the Drag and Flow Field of Two Bluff Bodies Separated by a Gap," *Journal of Fluid Mechanics*, Vol. 156, July 1985, pp. 167—204.

[6]Pamadi, B. N., "Effect of Cross Flow Angle on the Lift and Drag Coefficients of a Noncircular Cylinder with Strakes," *Proceedings of the AIAA Applied Aerodynamics Conference* (Williamsburg, VA), AIAA, Washington, DC, June 1988, pp. 582–592.

[7]Polhamus, E. C., "Effect of Flow Incidence and Reynolds Number on Low Speed Aerodynamic Characteristics of Several Non Circular Cylinders with Application to Directional Stability and Spinning," NASA TR R-29, Sept. 1957.

[8]Holmon, J. P., *Experimental Methods for Engineers*, 2nd Ed., McGraw-Hill, New York, 1971, Chap. 3.

[9]Obasaju, E. D., "An Investigation of the Effects of Incidence on the Flow Around a Square Section Cylinder," *Aeronautical Quarterly*, Vol. 34, Nov. 1983, pp. 243–259.

[10]Schlichting, H., *Boundary Layer Theory*, 6th Ed., McGraw-Hill, New York, 1968, pp. 20–21.